Multi-Instrument Observations of a Geomagnetic Storm and its Effects on the Arctic Ionosphere: A Case Study of the 19 February 2014 Storm

Observations of a Geomagnetic Storm

Durgonics, Tibor; Komjathy, Attila; Verkhoglyadova, Olga; Shume, Esayas B.; von Benzon, Hans-Henrik; Mannucci, Anthony J.; Butala, Mark D.; Høeg, Per; Langley, Richard B.

Published in:
Radio Science

Link to article, DOI:
10.1002/2016RS006106

Publication date:
2017

Document Version
Peer reviewed version

Multi-Instrument Observations of a Geomagnetic Storm and its Effects on the Arctic Ionosphere: A Case Study of the 19 February 2014 Storm

Tibor Durgonics*[1,2], Attila Komjathy[2,3], Olga Verkhoglyadova[2], Esayas B. Shume[2,4], Hans-Henrik Benzon[1], Anthony J. Mannucci[2], Mark D. Butala[5], Per Høeg[1], and Richard B. Langley[3]

[1] Technical University of Denmark, National Space Institute (DTU Space), 327-328 Elektrovej, Kongens Lyngby, Denmark.
(e-mail: tibdu@space.dtu.dk)

[2] NASA Jet Propulsion Laboratory, 4800 Oak Grove Dr, Pasadena, CA, USA.

[3] Dept. of Geodesy and Geomatics Engineering, University of New Brunswick, Fredericton, N.B., Canada.

[4] Astronomy Department, Caltech, Pasadena, CA, USA.

[5] University of Illinois at Urbana-Champaign, Champaign, IL, USA.

Abstract

We present a multi-instrumented approach for the analysis of the Arctic ionosphere during the 19 February 2014 highly complex, multiphase geomagnetic storm, which had the largest impact on the disturbance storm-time (Dst) index that year. The geomagnetic storm was the result of two powerful Earth-directed coronal mass ejections (CMEs). It produced a strong long lasting negative storm phase over Greenland with a dominant energy input in the polar-cap. We employed GNSS networks, geomagnetic observatories, and a specific ionosonde

This article has been accepted for publication and undergone full peer review but has not been through the copyediting, typesetting, pagination and proofreading process which may lead to differences between this version and the Version of Record. Please cite this article as doi: 10.1002/2016RS006106

station in Greenland. We complemented the approach with spaceborne measurements in order to map the state and variability of the Arctic ionosphere. In situ observations from the Canadian CASSIOPE (CAScade, Smallsat and IOnospheric Polar Explorer) satellite's ion mass spectrometer were used to derive ion flow data from the polar cap topside ionosphere during the event. Our research specifically found that, (1) Thermospheric O/N2 measurements demonstrated significantly lower values over the Greenland sector than prior to the storm-time. (2) An increased ion flow in the topside ionosphere was observed during the negative storm phase. (3) Negative storm phase was a direct consequence of energy input into the polar cap. (4) Polar patch formation was significantly decreased during the negative storm phase. This paper analyzes the physical processes that can be responsible for this ionospheric storm development in the northern high-latitudes. We conclude that ionospheric heating due to the CME's energy input caused changes in the polar atmosphere resulting in N_e upwelling, which was the major factor in high-latitude ionosphere dynamics for this storm.

Index terms: Auroral ionosphere, Ionospheric disturbances, Ionospheric dynamics, Ionospheric storms, Polar cap ionosphere

Keywords: Total electron content, Scintillations, GNSS, Ionograms, Geomagnetic storms, High-latitude ionosphere

1. Introduction

In this paper we focus on ionospheric storm disturbances in the Arctic ionosphere. The impact of geomagnetic storms on the ionosphere and the underlying first principles behind these physical and chemical processes have been discussed by numerous authors, including,

e.g., Rodger et al. [1992], Buonsanto [1999], and Blagoveshchenskii [2013]. Nevertheless, the precise geophysical background behind this complex system is still not completely understood [e.g., Lastovicka, 2002]. Coronal mass ejections (CMEs) and other manifestations of solar activity can trigger magnetospheric storms that may cause global or regional geomagnetic disturbances impacting the ionosphere. These effects will result in changes in the regular (e.g., diurnal, seasonal) ionospheric processes [e.g., Blagoveshchenskii, 2013; Durgonics et al., 2014].

Interaction between a CME and the magnetosphere often starts with the arrival of a shock wave in near-Earth space. On Earth's surface the outset of such interaction is seen as the sudden impulse (SI), which can be detected using, for example, geomagnetic field horizontal (H) component measurements collected by magnetometers. There is a set of well-established indices to identify the early stages of these interactions including the global disturbance storm time (Dst) index [e.g., Anderson et al., 2005; Le et al., 2004; Blagoveshchenskii, 2013], or the regional auroral electrojet (AE) index which is derived from auroral region magnetic stations and the polar cap north (PCN) index computed from a near-pole single magnetic station (details on the indices can be found in, e.g., Wei et al. [2009] and Vennerstrøm et al. [1991]). A sudden decrease in the Dst values typically indicates a change in the globally symmetric and asymmetric (partial) components of the ring current suggesting a global geomagnetic event [Liemohn et al., 2001]. Once such an event is identified, the local state of the geomagnetic field can be observed using data from the individual magnetic observatories in the Arctic region. The localized measurements can provide additional insights into the electromagnetic response to storm input, since the Dst is derived from a global network of stations with local information content no longer overtly present. These observed magnetic disturbances indicate dependence on the quasi-dipole (QD) coordinates [Emmert et al., 2010].

Ionospheric storms caused by geomagnetic activity can be observed using total electron content (TEC) scintillations based on global navigation satellite systems (GNSSes) observations, ionosonde observations, and other independent measurements of the ionospheric plasma [Pi et al., 1997]. The locations of a subset of GNSS stations used in this research, and a sample TEC map generated from the observed data are shown in Figure 1. Blagoveshchenskii [2013] and Schunk and Nagy [2009] described a set of variables to define the state of the ionosphere during storm-time conditions. These variables include season, local time, solar activity, storm onset time (or time-since-storm-onset-time), storm intensity, pre-storm state, and QD latitude. Additionally, ionospheric processes have to be considered along with processes of other regions of the geospace environment such as thermospheric circulation, neutral and ion composition changes, gravity waves, acoustic waves, chemical composition, variations in the electric and magnetic fields, and other couplings with the magnetosphere and neutral atmosphere [Heelis, 1982; Khazanov, 2011]. During such an ionospheric storm, there can be both positive and negative TEC anomalies (also known as phases) due to storm effects of different scales. The durations of the positive and negative phases typically exhibit a clear latitudinal dependence (i.e., at higher latitudes the negative phase is prolonged) and seasonal dependence (i.e., negative storms are more pronounced in the winter) [Mendillo, 2006; Mendillo and Klobuchar, 2006]. These phases are apparent in electron density (N_e) variations in the F2 layer (NmF2) and the changes in F2 peak height (hmF2) [Buonsanto, 1999]. In addition to electron density observations (describing the spatial distribution of the free electrons), ionospheric scintillation measurements can also be carried out to provide complementary statistics about irregular structures in the ionosphere, which are often accompanied by rapid signal phase fluctuations. This could be of particular interest in regions where polar patches are present [Prikryl et al., 2015]. A comparison of such N_e and scintillations in the Arctic region is performed in this paper, followed by analyses of the

results with particular attention to distinguishing between plasma gradients due to solar ionization and patches. Rate of TEC index (ROTI) will be presented as a surrogate indicator of ionospheric structure variations [Pi et al., 2013].

The purpose of the research is to observe and interpret the processes in the Arctic ionosphere, which are caused by CME-driven storm of 19 February 2014. During the course of this ionospheric storm the Dst index dropped to its lowest value of -95 nT in all 2014; additionally the related geomagnetic storm was highly complex. Therefore, we selected this specific event for our case study. For details on this specific storm see E. J. Rigler (unpublished data, 2014) available from the U.S. Geological Survey (http://geomag.usgs.gov/storm/storm18.php). In this research we investigate storm effects in ionospheric TEC and the vertical N_e and use scintillations during storm time as a key diagnostic tool.

The paper is organized as follows: Section 2 describes the storm effects of the 19 February 2014 ionospheric storm and the utilized methodology and instrumentation. In Section 3 we elaborate on the specific observation types and measurements. Section 4 introduces a scintillation index that originates from the same observations as TEC and may be combined with electron density results; this approach is able to provide further insights into temporal variations of the ionosphere and its smaller scale structure. In Section 5 we provide a summary for the research and draw conclusions in order to ascertain geophysical insights into the observed phenomena.

2. Methods, Instrumentation, and Observations

In this section we describe the storm effects, followed by an overview of the methodology, the instruments used, and the results of the different observations employed in the study. We start with the solar wind parameters and induced geomagnetic variations. This is followed by

an analysis of electron density observations and related neutral gas composition changes. Lastly, supporting data derived from TEC mapping, the Super Dual Auroral Radar Network (SuperDARN), and the CASSIOPE satellite ion mass spectrometer are presented.

2.1 Storm Effect Overview

At northern latitudes the auroral zone (or auroral oval) is typically located between 10 and 20 degrees from the geomagnetic pole and it is 3 to 6 degrees wide. Its location and width normally depend on the actual geomagnetic activity. The auroral zone expands and becomes wider during geomagnetic storms and subsequently contracts as the storm subsides [Feldstein, 1986]. Poleward from the auroral oval lies the polar-cap region, where the geomagnetic field lines are open and extend into space. Figures 2, 3 and 4 give an overview of the 19 November 2014 storm effects over Greenland. Figure 2 demonstrates how the solar wind parameters and vertical TEC (VTEC) values evolved over time (from 17-21 November 2014; for more see Section 2.2). Figure 2 shows a clear separation between polar-cap stations and auroral oval stations described below. Station Qaqortoq (QAQ1) indicates a strong negative storm phase onset on 18 February with the AE index concurrently showing an increased activity. AE indicates the strength of the auroral electrojet and it increases when the B_z and Dst begins to decrease around 14:00 UTC on 18 February. The solar wind proton density also shows activity at this time, ~10 cm^{-3}, and then it diminishes and only shows increased values again when the first CME impacts [Ghamry et al., 2016]. Station Sisimiut (SISI) can be either under the polar cap or the auroral oval, depending on geomagnetic and storm conditions. Panels 6 to 9 of Figure 2 show that the ionosphere above Sisimiut appears to be more similar to Qaqortoq than the other two stations at higher latitudes. The ionosphere over Upernavik and Thule on the other hand demonstrates clear polar-cap-like behavior, showing an abrupt TEC decrease while the PC index displays a sudden large energy input

into the polar-cap region coinciding with the first CME impact around 03:00 UTC on 19 February. After that time all stations exhibit negative storm effects with diminished TEC values for several days. For a comprehensive analysis of the solar wind parameters during the 19 February, 2014 storm see Ghamry et al., [2016].

2.2 Ground-Based Measurements and Solar Wind Parameters

Greenland's GNSS ground stations present a unique opportunity to observe the high-latitude ionosphere. Due to Greenland's unique location the ground-based GNSS measurements will cover regions representing the polar cap and auroral oval of the ionosphere providing a complete latitudinal profile of the Arctic ionosphere. GNSS ionospheric pierce points (IPPs) can be acquired ranging approximately from 55 to 90 degrees northern geographic latitudes and 10 to 80 degrees western longitudes. Measurements used in this work consist of 1-second, 15-second, and 30-second sampling interval using GNSS observations acquired from the Greenland GPS Network (GNET) permanent ground stations located along the Greenland coastline; see Madsen, F. B. (unpublished data, 2013) available from the Technical University of Denmark (http://www.polar.dtu.dk/english/Research/Facilities/GNET). The geodetic GNSS receivers are capable of tracking several observables, such as pseudorange observables (P1 or C1and P2), phase observables (L1, L2), and carrier-to-noise-density ratios (S1 and S2). We calculated TEC and related parameters using two independent methods and validated them against each other. The first method utilized the Jet Propulsion Laboratory's Global Ionospheric Maps (JPL GIMs); for details on JPL GIM see, e.g., Vergados et al. [2016] and Mannucci et al. [1998]. The second method was developed at the Technical University of Denmark's Space Department (DTU Space), and known as Arctic Ionospheric Map (AIM) with an overview of the processing steps described in the following section.

The GPS geometry-free combinations of phase and pseudorange (L_I, P_I) were calculated for each satellite-receiver pair as described by, e.g., Hernandez-Pajares et al. [2007]. The pseudorange observables were smoothed using a Hatch-filter approach [Hatch, 1982] and corrected for satellite and receiver differential code biases (DCBs). The TEC calculation has included the DCB values; for details see the equations in Hernandez-Pajares et al. [2007]. These slant TEC (STEC) measurements exhibit a pronounced elevation-angle-dependence since at different satellite elevation angles the length of the signal path through the ionosphere increases with lower elevation angles [Hernandez-Pajares et al., 2007]. To account for this effect an elevation-angle-dependent scaling scheme was applied in addition to a 10-degree elevation cut-off angle to minimize the effects of multipath error at low elevation angles. Both the type of weighting functions and the elevation cut-off angles were selected after evaluating several different options. Various 1/cosine-type weighting functions (or mapping functions) are commonly found in the literature. We adopt the standard thin-shell mapping function (e.g., Jakowski et al. [2011]; see also Mannucci et al. [1999] and references therein). Due to geography, a large number of the GNSS stations used in this work are capable of receiving signals directly from intercepting the polar-cap region. On the other hand the southernmost Greenland stations were actually located at mid-latitudes.

STEC and VTEC values are typically given in TEC units (TECU). One TECU is defined as 10^{16} electrons in 1 m^2 cross-section column along the signal path. The computed TECU values serve as a basis for our interpolation and two-dimensional (2D) TEC mapping. The data point locations for the interpolation are the geographic coordinates where the signal path pierces the single-layer model thin shell (this is a rotational ellipsoid in AIM and sphere in GIM) that represents the ionosphere, also known as IPPs. The IPPs form a 2D irregular grid. During the storm days the number of IPPs over Greenland was typically between 150 and 200 at each measurement epoch, depending on the number of receivers tracking and

ionospheric conditions. During high scintillation phases with storm time periods, the number of available IPPs is typically lower due to the increased number of cycle slips, which typically deteriorates data quality. Short satellite arcs are often impacted by carrier-phase cycle slips and depending on the size and location of the phase breaks, often the short arcs need to be discarded by the data processing software. Any VTEC values between ionospheric observations at IPP locations have to be estimated using an interpolation scheme. In this work we applied a natural neighbor interpolation scheme [Sibson, 1981]. For further details on VTEC interpolation and mapping see Durgonics et al. [2014]. The 2D TEC map color scales are consistent throughout the work to allow comparisons among different figures. In addition to the 2D VTEC maps in this research we also employ VTEC time series to obtain an overview of ionospheric diurnal variability locally, in the vicinity of a given station. At any one epoch, the MVTEC is calculated as the mean of all the VTEC values obtained from individual data points for a single station. Furthermore, a 10-degree elevation cut-off angle was applied throughout and so low elevation angle satellites are removed to minimize error sources such as multipath and to decrease the noise level. In our approach we used the same weight for each satellite. In addition, MVTEC represents a smoothed ionospheric single-layer surface over the given station while its standard deviation indicates how uniformly the ionosphere tends to behave in that region.

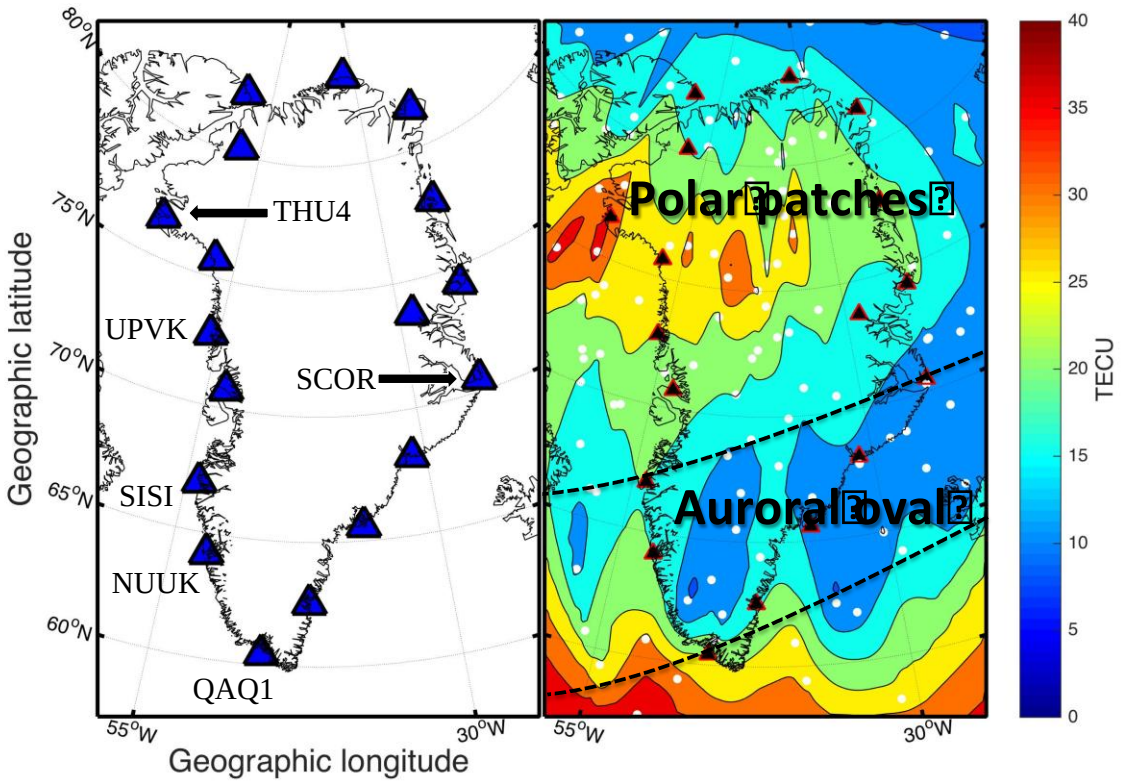

Figure 1. (left-panel) Map of Greenland with blue triangles marking the locations of a subset of GNET GNSS stations that has been used to generate the VTEC maps in this study. Six out of the 18 stations were specifically labeled so their locations will be easily identified in later figures. Legend for the station codes are as follows: Nuuk (NUUK), Qaqortoq (QAQ1), Scorebysund (SCOR), Sisimiut (SISI), Thule (THU4), Upernavik (UPVK). Note that the Thule ionosonde station is collocated with the Thule GNSS station for all practical purposes. **(right-panel)** An example for VTEC map over Greenland at 19:15:00 (UTC), 18 February 2014, the day before the CME impact. The VTEC values at the ionospheric pierce points are denoted with white circles. The mapping was performed by employing the commonly used natural neighbor interpolation scheme to estimate values using the IPP values. The map clearly demonstrates local ionospheric structures (see, e.g., [Rodger et al., 1992]) and polar patches . Due to the experimental setup auroral-E ionization (AEI) is not clearly apparent in this figure (for further details on AEI detection see Coker et al. [1995]). The auroral oval

boundaries for this particular time are taken from The John Hopkins University Auroral Particles and Imagery website (http://sd-www.jhuapl.edu/Aurora/ovation/ovation_display.html).

The GNSS instruments employed in this work also allow us to study ionospheric scintillations via ROTI. Scintillation indices typically quantify temporal variances of the signal phase and amplitude caused by variations in index of refraction along the signal path. The refractive index is a function of N_e. Therefore scintillation indicates the presence of electron density gradients. During disturbed times ionospheric scintillations can be severe. The scintillations and their characteristics vary as a function of amplitude, phase, polarization, and angle of arrival of the signal [Maini and Agrawal, 2011]. ROTI is a suitable occurrence indicator for L-band ionospheric scintillations and for the current work it may have advantages over the traditional scintillation indices, i.e., phase scintillation (σ_φ) and amplitude scintillation (S_4) indices. ROT and ROTI can be computed from the same data source as TEC using L1 and L2, the corresponding wavelengths ($\lambda_{1,2}$) and frequencies ($f_{1,2}$) using the following equations,

$$ROT(t) = \frac{L_I(t) - L_I(t-\Delta t)}{40.3\ 10^{16}\ \Delta t\ (\frac{1}{f_1^2} - \frac{1}{f_2^2})}, \quad (1)$$

where *ROT* is in TECU/min units, *t* and Δt are the time at any epoch in minutes and the sampling interval (1 sec in present work), respectively. *ROTI* is the de-trended standard deviation of *ROT* over *N* epochs, i.e.,

$$ROTI(t) = \sqrt{\frac{1}{N}\sum_{t-N}^{t}(ROT(t'-N) - \overline{ROT})^2}, \quad (2)$$

which is calculated using a 1-minute running window [e.g., Pi et al., 2013; Jacobsen, 2014]. GNET consists of geodetic GNSS receivers that produce data well-suited for ROTI calculation. This is not the case for the traditional indices (i.e., $\sigma_{\varphi,}$ S_4) that are typically derived from single frequency phase and power measurements at high cadence (50 Hz or higher), and are usually better handled by specialized ionospheric receivers. Although the relationship between the magnitudes of ROTI and σ_φ is not linear, according to Pi et al. [2013], ROTI is very well correlated with σ_φ, which is the prominent scintillation index used in the Arctic region [Pi et al., 1997 and 2013]. This is due to the fact that at these latitudes, the high-speed plasma convection suppresses S_4 due to the Fresnel filtering effect, while σ_φ remains independent of the Fresnel zone size [Mushini et al., 2014 and Kersley et al., 1988]. This analysis seems to break down when the plasma irregularity scales become larger than Fresnel scales, for strong turbulence cases. In addition, the minimum detectable plasma irregularity scale size depends on the sampling rate of the receiver. According to typical SuperDARN data (to be discussed subsequently), relative plasma drifts are of the order of 1000 m/s in the polar-cap region, which in theory requires at least 1-Hz sampling rate to detect 1-km-size irregularities. For more, see Virginia Tech SuperDARN (unpublished data, 2014) available from the Virginia Tech Data Inventory (http://vt.superdarn.org/tiki-index.php?page=Data+Inventory). The ROTI results presented in this work are generated from 1-Hz-sampled data (i.e., N = 60). There exist certain limitations to the applicability of ROTI, which have to be considered when interpreting ROTI results. Bhattacharyya et al. [2000] describes in detail that the phase screen approximation should be valid. This limitation does not hold for example for σ_φ. The limitations essentially mean that thick layers of irregularities might not be tracked sufficiently by ROTI.

Further ground-based measurements using ionograms and related ionosonde observations were acquired from the Greenlandic Thule ionosonde (Digisonde) station. This station

collects measurements every 15 minutes. The TEC provides integrated N_e values that can be mapped onto a horizontal geographic 2D surface, and the ionosonde data were used to determine the vertical 1D N_e distributions over the ground station. These two measurements may be considered completely independent of each other.

Additional ground-based measurements were acquired from a network of coherent HF radars (SuperDARN). It operates by continuously observing line-of-sight velocities, backscatter power, and spectral width from ~10-m-scale plasma irregularities in the ionosphere. SuperDARN data has been successfully used in combination with relatively low horizontal resolution TEC data in previous studies [e.g., Thomas et al., 2015 and Prikryl et al., 2015]. The higher resolution TEC data available from GNET in combination with SuperDARN convection maps presented in this work potentially allows for an improved monitoring of polar-cap patches and their time evolution in the Greenland sector.

Our method to identify time periods with disturbed ionospheric conditions was based on Dst, AE, and PCN indices (for a detailed comparison of these indices see, e.g., Vennerstrøm et al. [1991]) and geomagnetic horizontal north component measurements (see Figure 3 below). Preliminary identification of the beginning of CME-induced geomagnetic storms can be done through analysis of Dst data by detecting significantly negative peaks. On 18 February, Dst heads towards a temporary minimum of -70 nT while AE rises significantly (Figure 2), both classical signatures of a storm main phase [Blagoveshchenskii, 2013; Tsurutani and Gonzalez, 1997; Gonzalez et al., 1994]. High-resolution local magnetic data were acquired (magnetic H component measurements) from the Greenlandic network of magnetic stations, with relevant magnetic measurements shown in Figure 3. Some of the magnetic stations are in close proximity to GNSS stations and at some locations to ionosondes as well (e.g., Thule).

At this point it is worth pointing out that the sudden PCN rises on 19 and 20 February (near the red dotted lines A and B in panel six of Figure 2) coinciding with observed MVTEC depletions in the data of polar cap GNSS stations in Thule and Upernavik (Figure 2, panels 7 and 8) . The same electron density depletions may be less noticeable for auroral oval stations in Sisimiut and Qaqortoq (Figure 2, panels 9 and 10). More on the electron density observations can be found in Section 2.3.1.

The ground-based magnetic instruments consist of 1 Hz sampling rate capable vector variometers. The local magnetic coordinate system is oriented along local magnetic north and east at the time of the vector variometer instrument setup and adjusted every year. In Figure 3, the horizontal north component changes are shown for 19 February 2014.

2.2.1 Analysis of Solar Wind Parameters and Geomagnetic Observations

The storm was highly complex and had multiple main and recovery phases resulting from a series of Earth-directed CMEs (see http://geomag.usgs.gov/storm/storm18.php and Ghamry et al. [2016] for details). As shown in Section 2, Dst, AE, and PCN are all geomagnetic indices but there are also fundamental differences among them. For a more complete discussion see, e.g., Vennerstrøm et al. [2011]. The local magnetometer measurements shown in Figure 3 are more comparable to PCN and AE while Dst is sensitive to the ring current, which exists due to larger-scale (global) magnetospheric convection patterns. This fundamental difference has to be taken into account when interpreting and comparing local, regional, and global indices, such as ones discussed before in Section 2.2.

The magnetic disturbances in Figure 3 indicate an approximately 1 hour propagation-based delay compared to the disturbance in the Dst. There appears to be an additional delay, with the disturbance propagating from south to north direction (there is a ~110 second delay between Nuuk and Thule). Note that the magnetic measurements (local north component and

Dst) are only applied as indicators of storm activity. There are several other phenomena occurring simultaneously that may also affect the geomagnetic field measurements including the ionosphere currents induced ground currents. The magnetic field north component sudden drop seems significant at stations Kangerlussuaq (located approximately 130 km east of Sisimiut, see Figure 1) and Nuuk, and they appear to show a very similar pattern in the Dst drop (compare Figures 2 and 3). The local recovery is however significantly faster than the Dst recovery. This was expected due to the fact that Dst is sensitive to significantly-larger-scale convection patterns than regional and local indices. While both stations registered the north component values at approximately 14:00 UTC, the Dst took several days to fully recover. During the same time, the observed magnetic north component at Thule demonstrated a significant increase in early onset rather than a decrease. This positive response was delayed by approximately 100 seconds compared to station Kangerlussuaq and after approximately 6 hours values of ~200 nT below the quiet level were observed (see Figure 3).

The Dst (shown in Figure 2) exhibited only a small main phase when the first CME's effect was observed, around 03:00 UTC on 19 February. Observed UTC times of the CME launch and the estimated times when the CMEs reached Earth's magnetopause were obtained from the USGS National Geomagnetism website (http://geomag.usgs.gov/storm/storm18.php).

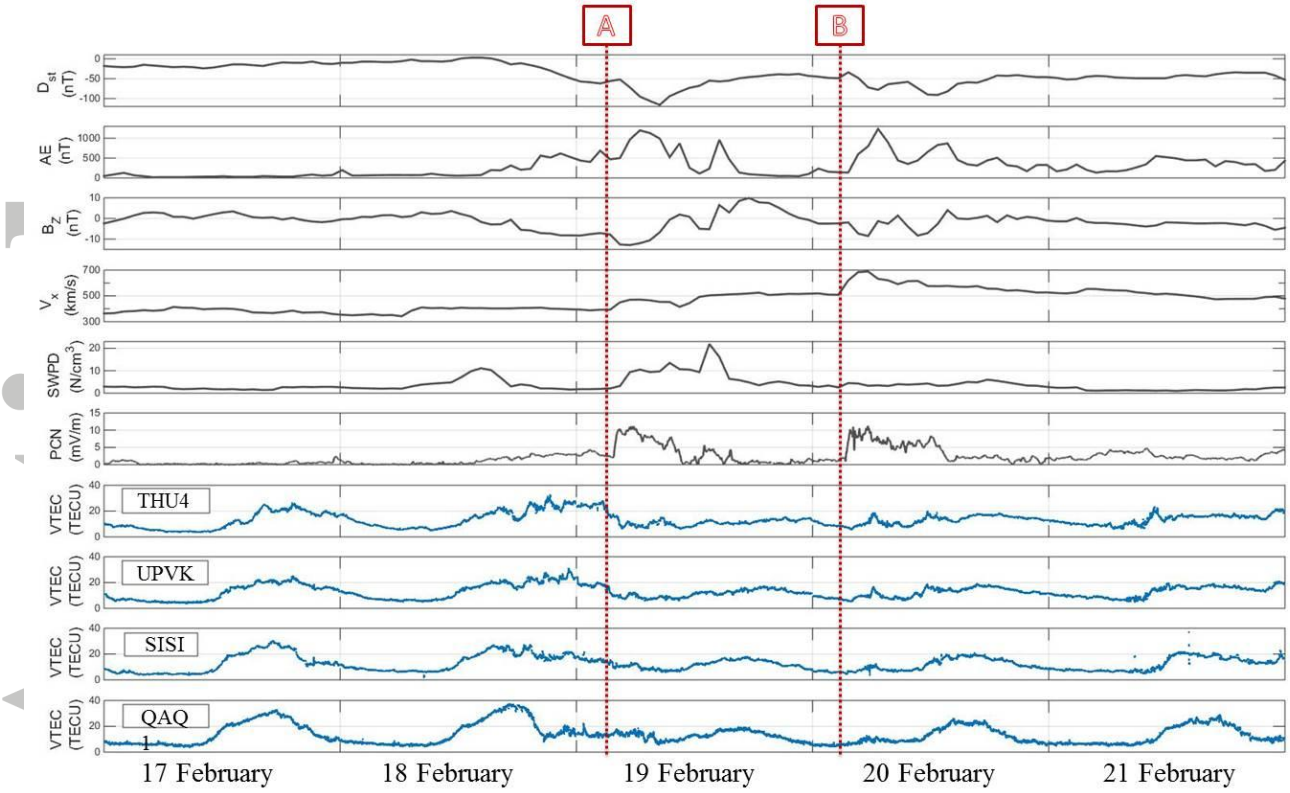

Figure 2. Near-Earth solar wind, interplanetary magnetic field (IMF), and plasma parameters shown in addition to the computed MVTEC using four Greenlandic GNSS stations on 17-21 February 2014: **(first panel)** Dst index, **(second panel)** AE index, **(third panel)** IMF B_Z component, **(fourth panel)** OMNI solar wind velocity *x* component, **(fifth panel)** OMNI solar wind proton density, **(sixth panel)** PC north index, **(seventh to tenth panels)** MVTEC values in order of decreasing station geographic latitude: Thule (77°28'00"N, 69°13'50"W), Upernavik (72°47'13"N, 56°08'50"W), Sisimiut (66°56'20"N, 53°40'20"W), and Qaqortoq (60°43'20"N, 46°02'24"W). The red dashed lines mark the approximate times when the first **(A)** and second **(B)** CME-induced effects were detected in the observations.

The Dst index eventually decreased by in excess of 100 nT. This was followed by a recovery phase, during which the Dst nearly recovered by about 50% of its earlier minimum in ~10 hours. The second CME's effect was detectable shortly after 03:00 UTC on 20 February.

This was followed by a much slower recovery phase lasting about 3 days. The local magnetic H component anomaly observed from local Greenlandic stations (Figure 3) showed an approximately one to two hours delay compared to the lowest Dst peak. However, the negative peaks also appeared in the local observations. One exception is for the magnetic data at station Thule, which in fact showed a positive magnetic H component anomaly during these events.

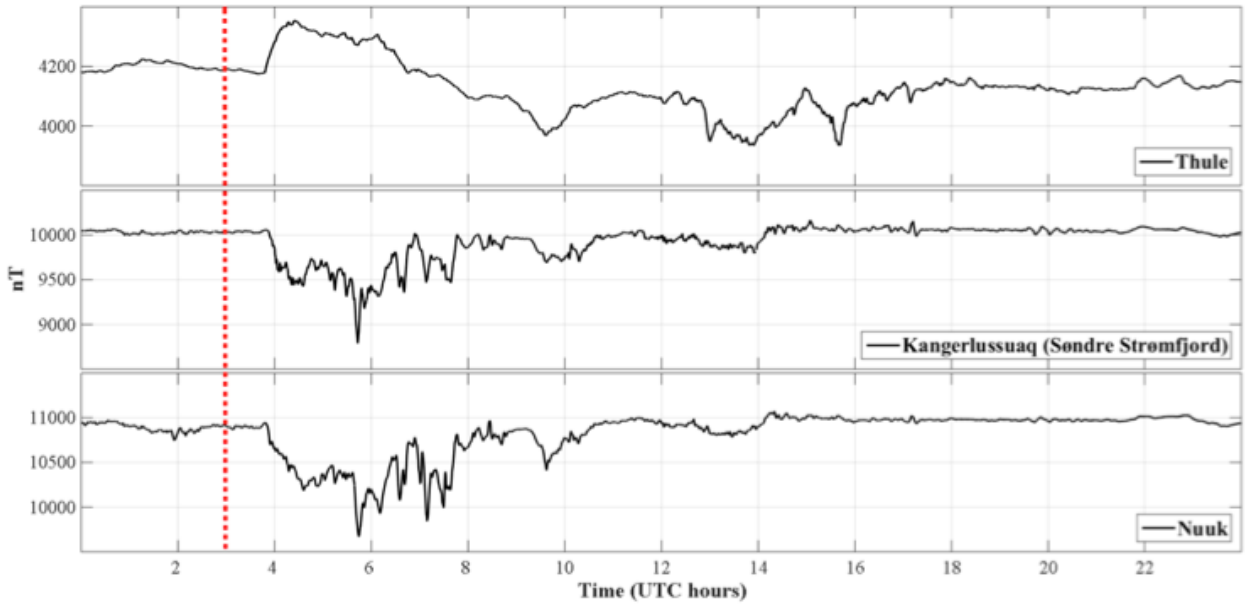

Figure 3. 1 Hz vector variometer measurements from Greenlandic ground stations of the magnetic field vector north component on 19 February 2014. Thule is the northernmost and Nuuk is the southernmost station among the three indicated in the figure. The USGS National Geomagnetism website estimated that the first CME reached the Earth's magnetopause around 03:00 UTC (marked by the vertical red dotted line). Among these three stations the Nuuk magnetic north component indicated the first changes, then ~10 seconds later they were observed at Kangerlussuaq, and finally ~100 seconds later they were observed at Thule. The timing accuracy of the instruments is ±2 seconds. The local ground magnetic response was delayed by almost 1 hour compared to the Dst drop.

2.3 Spaceborne Measurements

In addition to ground-based observations and solar wind parameters two spaceborne measurement types were analyzed to better understand the physical processes responsible for the observed storm effects. The first instrument is the Global Ultraviolet Imager (GUVI) on board the TIMED spacecraft providing global measurements of the far ultraviolet dayglow intensity [Paxton et al., 2004]. The observations allow the determination of atmospheric O/N_2 concentration changes that affect the level of ionization in the upper atmosphere. During storm conditions, the column density ratio $\Sigma[O/N_2]$ tends to decrease at high latitudes [e.g., Prölls, 1995; Verkhoglyadova et al., 2014; Meier et al., 2005; Zhang et al., 2004]. We analyzed GUVI O/N_2 ratios for two quiet days before the first CME, the day of the first CME hit, and for three additional days during the negative storm phase. The negative O/N_2 anomaly following the CME onset would indicate that the TEC negative storm may have resulted from atmospheric composition changes.

The second spaceborne measurement type was collected by the e-POP (Enhanced Polar Outflow Probe) instrument on board the Canadian CASSIOPE (CAScade, Smallsat and IOnospheric Polar Explorer) satellite. e-POP is a suite of eight scientific instruments that were designed to measure physical parameters related to space weather. CASSIOPE was inserted in a low-Earth polar orbit and, at the time of the storm, it had a ~325 km perigee and ~1456 km apogee. Its orbit inclination was 80.995 degrees [Yau and James, 2015]. All data presented here from CASSIOPE observations were measured along near perigee passes in the Arctic region. We used measurements from one of the eight instruments of e-POP, specifically the Imaging and Rapid Scanning Ion Mass Spectrometer (IRM). The IRM is a low-energy ion spectrograph, capable of measuring the energy, mass, and direction of arrival of incident ions in two- and three-dimensional scans in the energy range 1-100 eV/q, over ±180 degrees pitch angle, and ±60 degrees in azimuth angle, where q is the elementary

charge. The instrument performs an entire 2-D sample of the local ion population in 1/100 second, for an imaging rate of 100 Hz. For a detailed description of IRM instrumentation, measurement techniques, and data products see Yau et al. [2015]. During the observation window used in this work e-POP was in default mode, designated as "Addressed Mode" or AM. This mode normally generates data that are pairs of pixel-address and time-of-flight. For the purpose of this work we utilized the following datasets for IRM. They included TOF (Time-of-Flight) bin counts, angle-dependent pixel counts (360 degrees along pitch angle), and skin current. TOF is in units of bin periods each corresponding to 40 ns. The IRM instrument operates semi-autonomously gathering measurements in the form of detected anode pixel hits and respective TOF. The IRM pixel data consist of 16-bit values representing 6 bits identifying pixels and 10 bits representing the corresponding TOF for the detected pixel. Measured sensor skin current is also reported in the data packets together with the main instrument data [Yau et al., 2015].

2.3.1 Results: Electron Density Observations

Figure 4 shows the evolution of ionosonde-derived vertical N_e profiles (including the relation between their peak heights and integrated N_e values) and mean VTEC (MVTEC) time series during the 19 February 2014 geomagnetic storm over station Thule (THU4) in Greenland. These two observations provide the foundation to analyze the polar ionosphere dynamics during the storm. Due to the nature of the ground based ionosonde measurements the topside ionosphere needs to be modeled to obtain a full vertical profile resulting in our case modeled topside using a fitted Chapman profile. Following this topside modeling the ionosonde electron density profile can be translated into VTEC in TECUs directly over the station. This is done by integrating the ionosonde profile which is also given along a 1 m^2 column

similarly to the definition of the TEC. The major source of differences between ionosonde-derived TEC and GNSS-TEC (Figure 4, middle panel) originates from the inaccuracies in the topside modeling. On 17 and 18 November, the typical diurnal enhancements were building up in the F2 layer, which was interrupted by the storm after 03:00 UTC on the 19th in the polar-cap region and earlier in the auroral region. The diurnal variation during the 18th was barely distinguishable from typical diurnal activity of this particular season (or the day 17th), except for an apparent 3-5 TECU positive enhancement. This is just slightly above the TEC uncertainty, which is ±2.8 TECU for the AIM. AIM outputs result on an irregular grid, therefore its spatial resolution depends directly on the IPP distribution and its temporal resolution equals the sampling-rate of the GNSS data. The main source of this error seemed to result from the stations' differential code bias (DCB) estimations. The JPL GIM uncertainties are at the 2 TEC level in middle and high-latitudes and about 3 TECU for low-latitude regions [Komjathy et al., 2005a and Komjathy et al., 2005b]. The DCBs have lower uncertainties as GIM is estimating biases once a day assuming that receiver and satellite differential biases will not change over the course of one day. GIM uses Gauss-Markov Kalman filter taking advantage of persistence in the solar-geomagnetic reference frame constraining DCBs biases when separating hardware-related biases and elevation- angle-dependent ionospheric delays. [Vergados et al., 2016 and Komjathy, 1997]. GIM has a 1 degree by 1 degree native spatial resolution and a 15-min temporal resolution. Positive enhancement (phase), which builds up once the disturbance has arrived, was typically observed in the investigated events during 2014. This phenomenon is described in more details in, e.g., Mendillo [2006]. It may also appear in mid-latitudes, for instance as shown in Durgonics et al. [2014]. However due to the TEC error it cannot be fully confirmed without more precise measurements to be collected. The hmF2 turned out to be approximately 20-40 km higher during 18 February compared to 17 February. Shortly after 03:00 UTC (~

midnight local time) on 19 February when the first shock arrived there was a sudden drop in the TEC values, which was also apparent in the ionogram as a sharp contrast line. hmF2 became abruptly elevated by about ~150 km. Several hours later, during local daytime, following this, the F region showed significant depletions, the TEC fell to ~7 TECU and subsequently, hmF2 was elevated abruptly by about ~150 km. Several hours later, during local daytime, the F-region showed significant depletions. The TEC values fell to ~7 TECU where values of 20-25 TECU had been more typical. This period can clearly be observed in the ionogram plot shown in Figure 4. The diurnal variations only resumed after 16:00 UTC on 20 February; however the daily maximum values only reached a level of approximately ~10 TECU less than during calm days in this season. Furthermore, there was a gradual increase in the TEC values on 20 and 21 February. The daily TEC minima during the ionosphere recovery phase did not decrease compared to the calm day values, and yet they showed an apparent, slight (~2 TECU) increase, which falls within the error bar. Dst was gradually recovering in a somewhat similar fashion to the TEC (Figure 2). The ionosonde-derived VTEC is well correlated with GNSS TEC, but it shows a clear positive bias. This offset requires further studies, but it is possibly due to the topside model estimation of the ionosonde profiles and GNSS DCB estimation errors. NmF2 and hmF2 demonstrate a weak negative correlation amounting to -0.6.

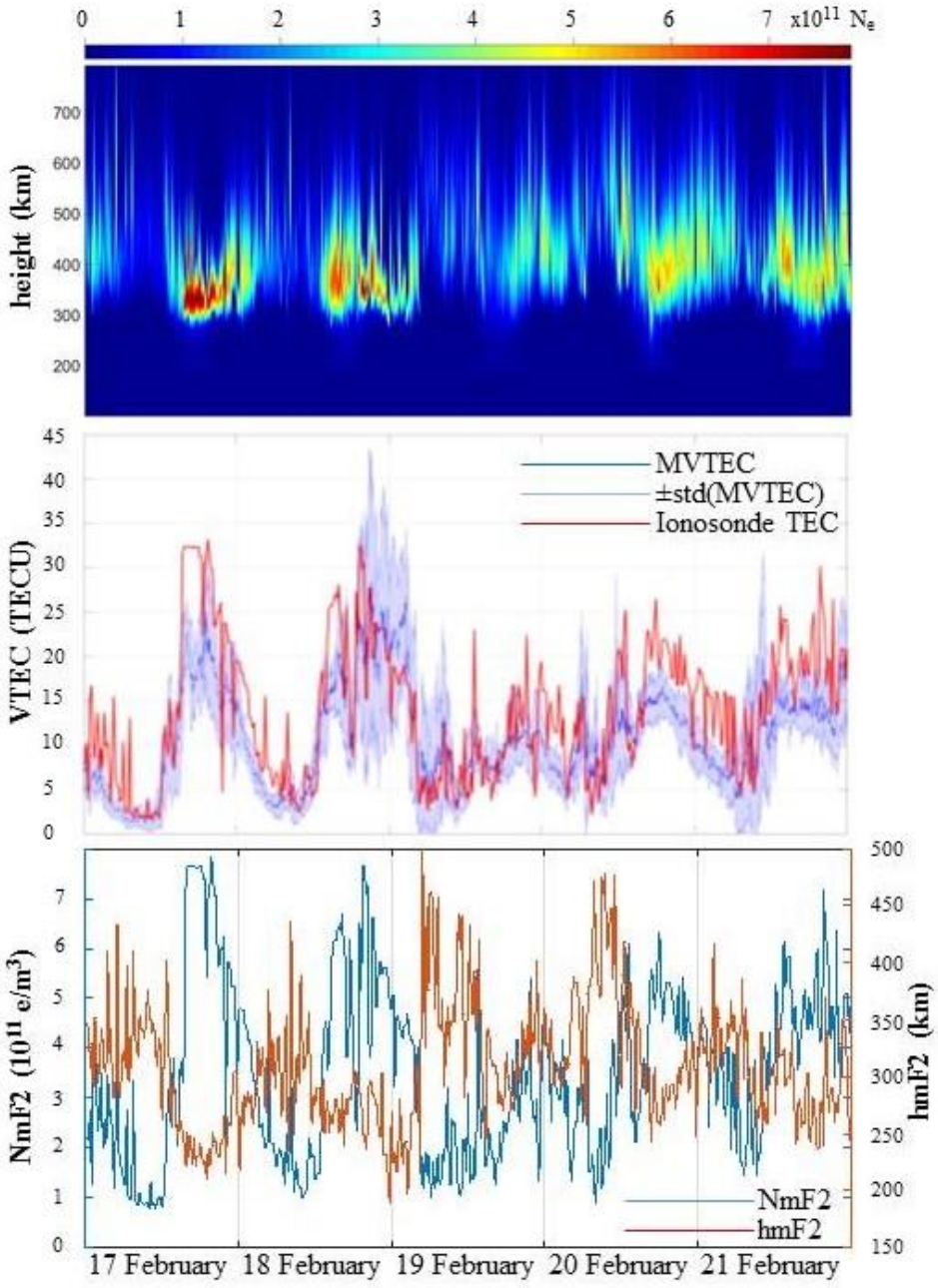

Figure 4. (top) Ionogram-derived profiles showing 5 days of ionospheric vertical N_e distributions observed by a digital ionosonde located at Thule. The measurements were collected at every 15 minutes. The N_e distributions show that the principal ionized region is the F layer with hmF2 typically around 300 km. **(middle)** MVTEC time series above Thule during the same days as shown in the top image (dark blue line) with the standard deviation of the MVTEC (light blue shading) and the ionosonde-derived TEC (red line). The diurnal

ionization cycle in the F-layer was disrupted after the first CME arrival. The TEC recovery occurs for several days similarly to the Dst (ring current) recovery (Figure 2). **(bottom)** NmF2 and hmF2 time series demonstrating negative correlation.

In order to further investigate the Arctic ionospheric N_e changes induced by CMEs we identified five further noteworthy (peak Dst <-65 nT) geomagnetic storms during 2014, and we analyzed two similarly prominent storms via the same methodology that we applied to the 19 February 2014 event. The 12 April 2014 and the 12 September 2014 events (the dates indicate the day when the Dst minimum occurred) resulted in very similar ionospheric storm effects; all three solar events triggered analogous disturbances in the ionosphere. The analyzed high-latitude ionospheric storms exhibited the following common characteristics (see Figure 4): (1) during the geomagnetic storm initial phase the regional TEC increased by ~3 to 5 TECU (just above the uncertainty level) compared to the previous calm periods, and (2) during the main phase, if it was not followed by a fast recovery phase (e.g., in Figure 4, during the second half of 19 February), the F layer was disrupted and the decreased ionization resulted in -10 to -20 TECU anomalies which lasted for days. When there was a fast Dst recovery phase (which is driven by the B_z component turning positive) during the several-days-long main recovery period, it resulted in a sudden increase in F-layer ionizations of about ~5 TECU for a short time (2-3 hours). Multiple sudden increases can be observed from 19 to 21 February. The long recovery period of the ionosphere is regional (it is present in the polar cap and the auroral oval, although their development is somewhat different see Figure 2) and lasts for days. Although it is the dominant factor in the regional TEC, there are still sub-regional inhomogeneities present (Figure 2).

2.3.2 O/N_2 Composition Changes

The column density ratio $\Sigma[O/N_2]$ maps (for more details, and technical background on the column density ratio maps, see, e.g., Prölls [1995]) for six consecutive days are shown in Figure 5. 17 February 2014 showed typical values over the extended study area followed by a slight decrease on 18 February 2014. On the day of the storm N_2 upwelling occurred over a large area mostly covering latitudes above 50 degrees. Details of the physical mechanism of atmospheric upwelling can be found in, e.g., Prölls [1995].

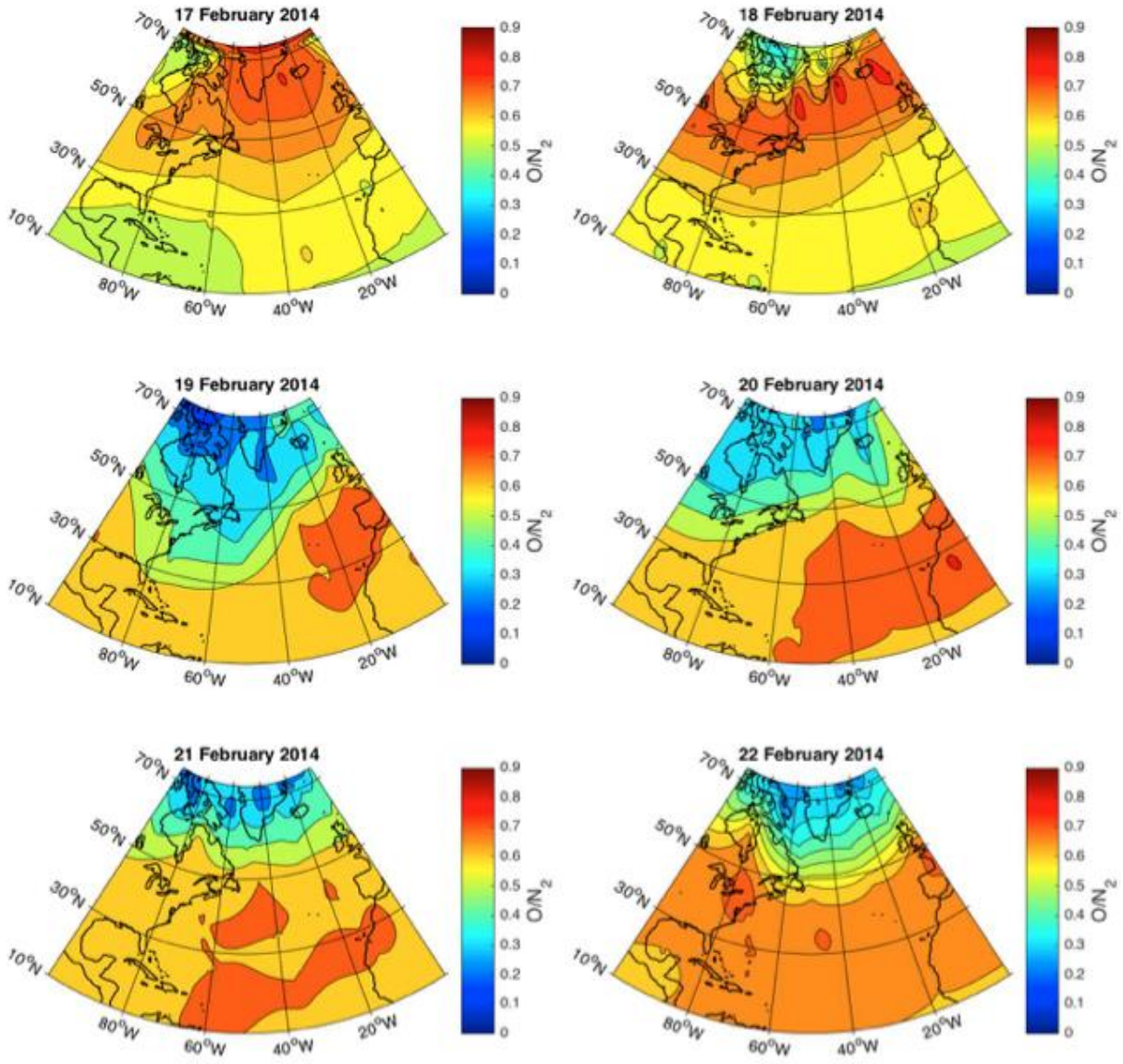

Figure 5. O/N_2 ratio maps demonstrating composition changes during the six days we investigated. The first CME hit on 19 February and the second on 20 February. The northernmost slice of these maps is shown in Figure 6.

O/N_2 ratios decreased to ~0.2-0.3. The negative anomaly lasted for several days recovering slowly to typical values prior to the disturbance (~0.7). Figure 6 displays global longitudinal slices of the GUVI-derived maps along 73 degrees latitude with Greenland located approximately between 30 and 60 degrees west longitude.

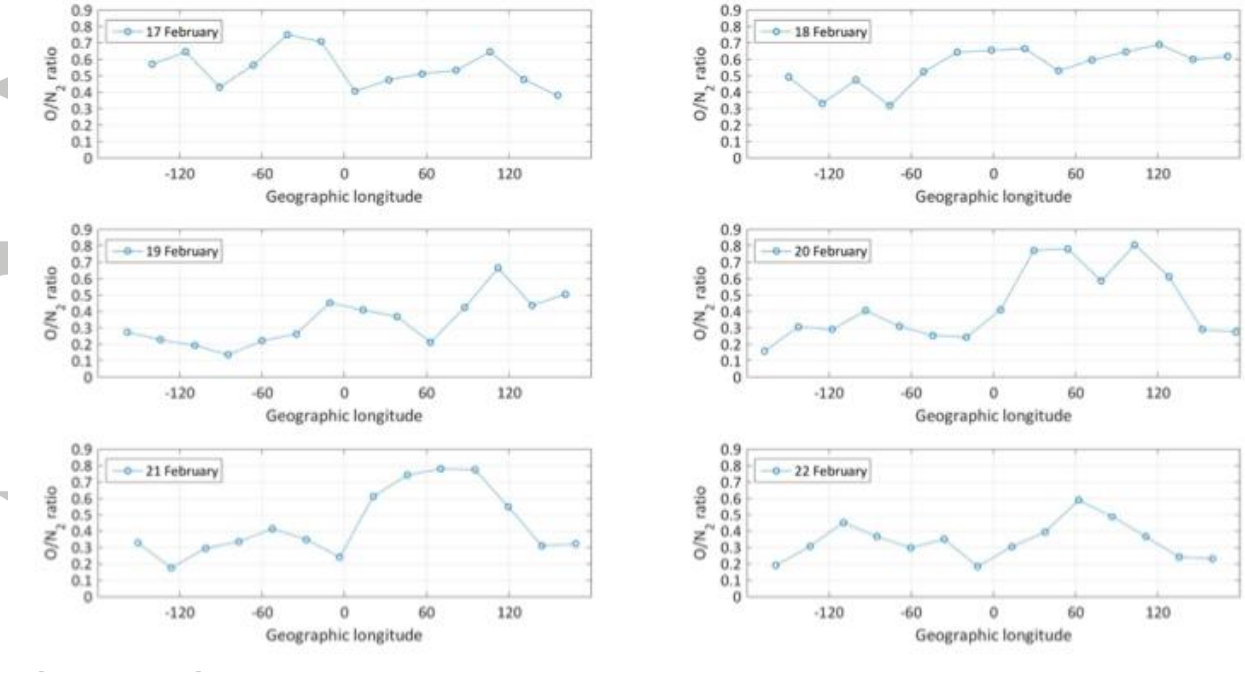

Figure 6. Longitudinal profiles demonstrating O/N_2 ratios (unitless) along 73-degree north latitude. The first CME hit on 19 February and the second on 20 February.

Typical values prior to the storm event were around 0.7 to 0.8. On the day of the storm the values decreased to ~0.3. The recovery period lasted for several days similarly to the TEC recovery (Figure 5).

2.3.3 Polar Patch Propagation and Convection

Figure 7 shows collocated convection and contours of magnetospheric electric field potentials from SuperDARN and GNSS-derived VTEC at 23:30 UTC on 18 February 2014.

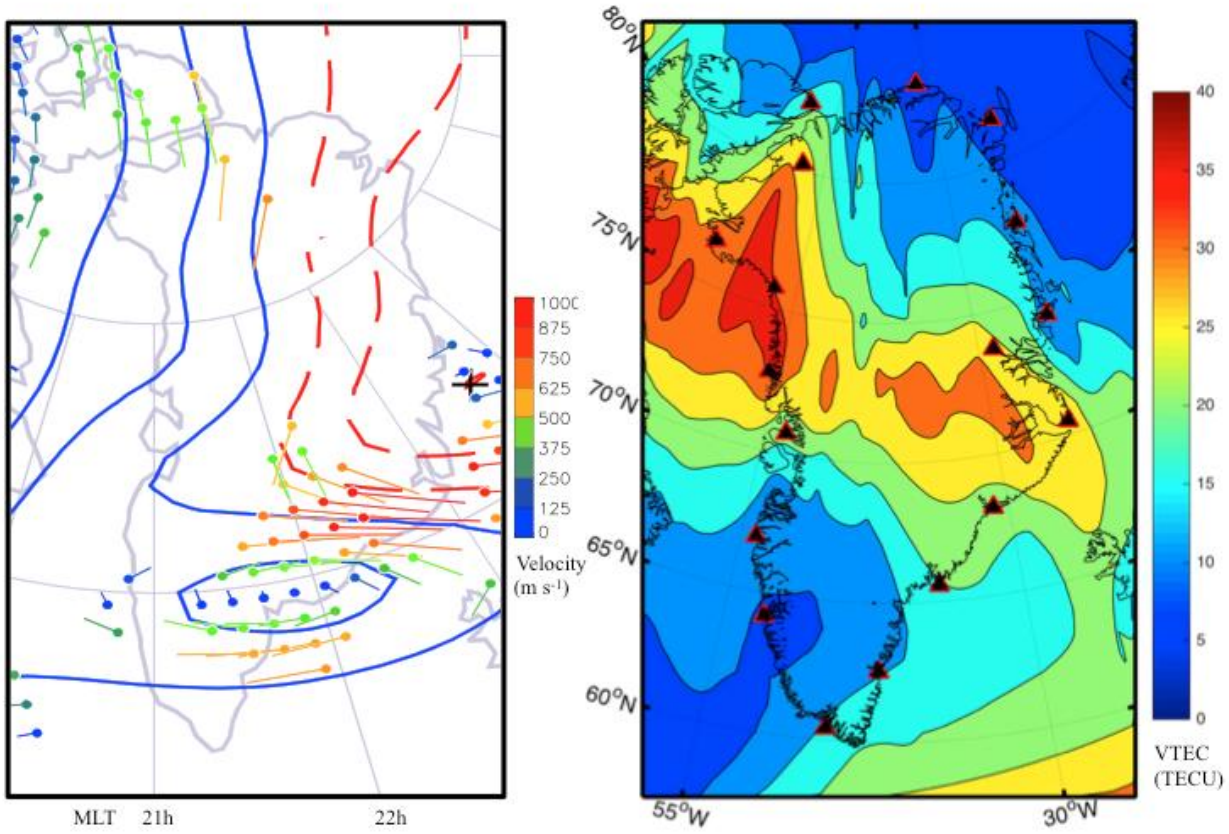

Figure 7. (left) SuperDARN drift velocities and contours of magnetospheric electric field potentials shown at 23:30 UTC on 18 February 2014 based on SuperDARN. The region between the two-cell convection pattern is located over Greenland (between red and blue potential contours). Anti-sunward convection of mid-latitude-originated plasma is drifting over the polar cap there (when B_z points downwards as shown in Figure 2). The closed blue contour surrounds a stagnation zone that results in increased plasma decay; compare this area with the same location on the right panel. **(right)** VTEC map covering the same geographical extent as the left panel. It was derived using 18 GNSS stations (black triangles

with red edge) in Greenland. The interpolation is made from approximately 200 IPPs. The figure clearly shows connected, but non-uniform patches near the inter-cell, anti-sunward convection zone.

Comparison of the left and right panels of Figure 7 demonstrates that TEC values tend to be low in stagnation zones (Figure 7, left panel), where drift speed is low and high where the anti-sunward plasma drift is dominant. The anti-sunward direction can be determined by the magnetic local time (MLT) values in Figure 7, left panel. Figure 8 shows time evolution of polar-cap patches during a 30-minute time interval [Rodger et al., 1992].

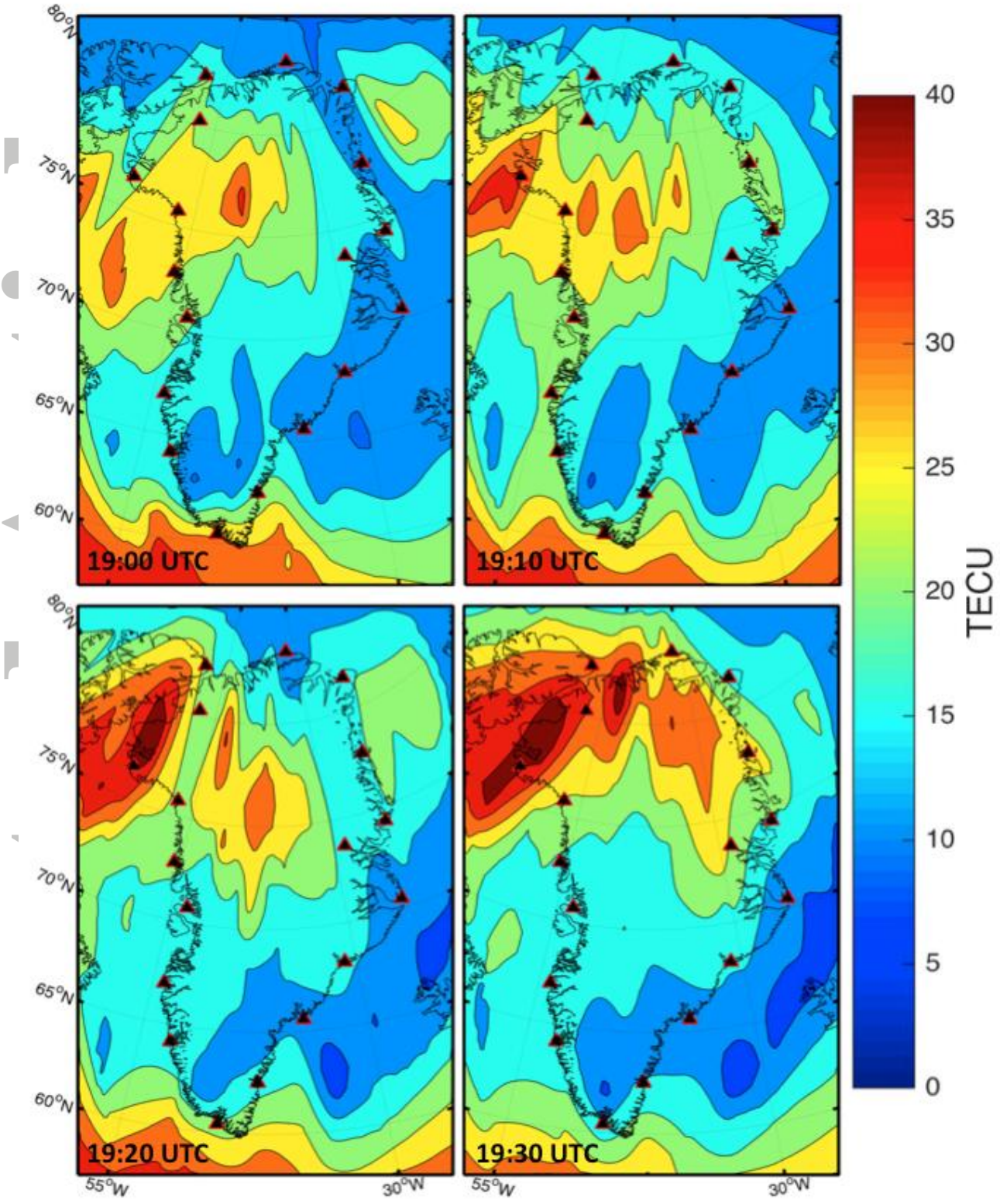

Figure 8. Polar patch structure progression over time shown from 19:00 to 19:30 UTC on 18 February 2014. The panels represent 10-minute increments. The negative TEC anomaly along 65 degrees latitude lies between the polar-cap convection zones and the mid-latitude ionosphere.

Velocity magnitudes calculated from features in the TEC data appear to be in good agreement with SuperDARN magnitudes. The observed polar-cap patches shown in Figure 8 are typically propagating with velocities between 500 and 1000 m/s. During this period, the B_z component was negative (Figure 2) and the anti-sunward cross-polar-cap convection seemed dominant in the region. The TEC mapping reveals connected patch structures and individual patches drifting in lower electron density regions, as well.

2.3.4 Ion Composition and Velocity Distribution of Ions in the Topside Ionosphere

Topside sounding of ion physical properties was feasible using the IRM sensor on e-POP. The altitudes of CASSIOPE were between 350 and 650 km in the Arctic region when taking the measurements. IRM is capable of distinguishing between the five most abundant ion species in the topside ionosphere including H^+, He^+, N^+, O^+, and NO^+. An important parameter that affects the pixel and TOF separation of the IRM instrument data is the hemispherical electrostatic analyzer (HEA) inner dome bias voltage (V_{SA}) [Yau et al., 2015]. Due to the fact that the highest energy ions arrive at the outermost portion of the detector the energy range of the detected ions depends primarily on V_{SA}. For a detailed description of the detector geometry and voltages interested readers are referred to Yau et al. [2015]. The V_{SA} value can be set between 0 and -353 V. By using different values one can achieve different separations between the detection of the aforementioned ion species. Time-of-flight versus time (TOF-t) and energy-angle versus time (EA-t) measurements are shown during four different passes in Figure 9.

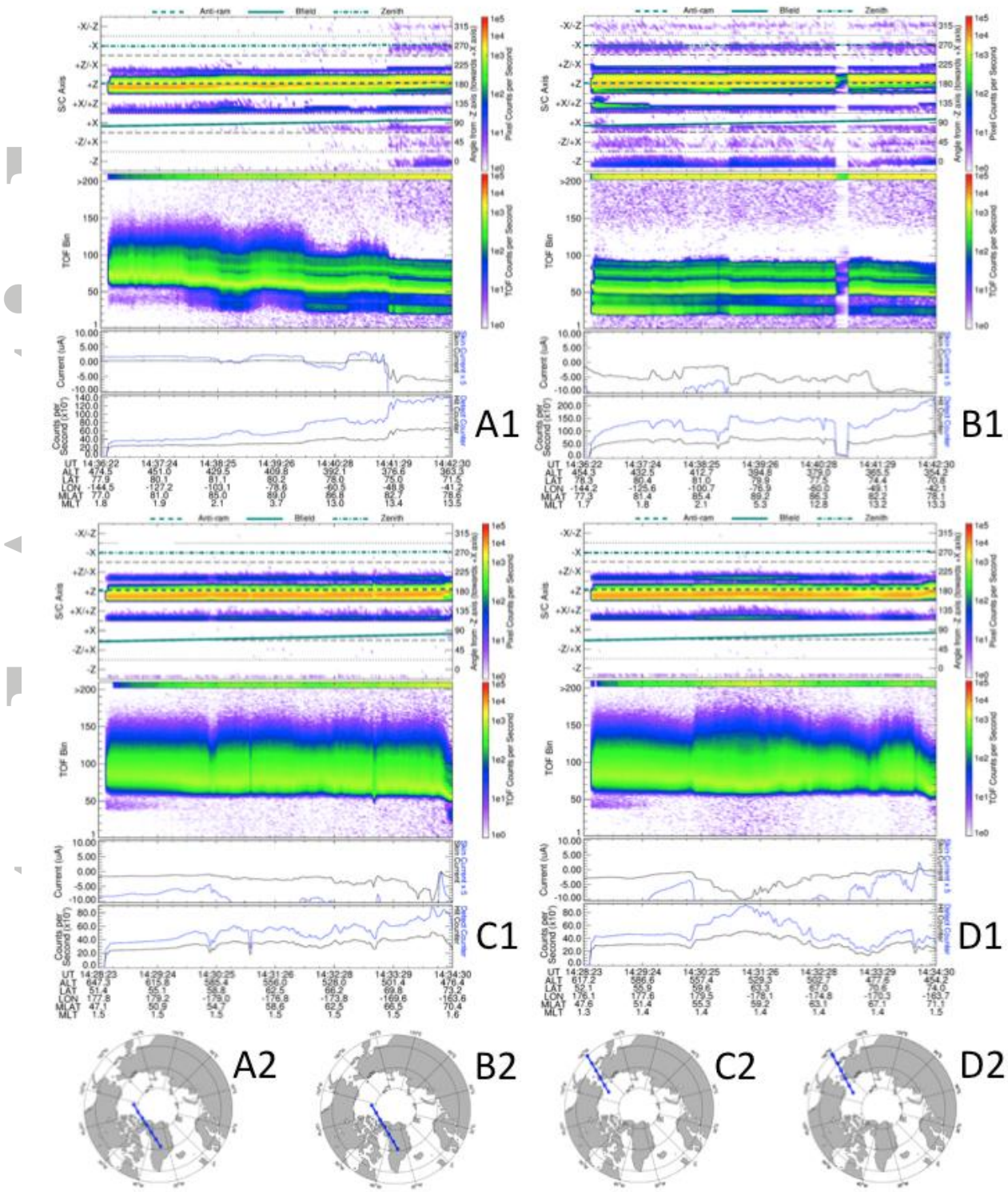

Figure 9. Measurements acquired from four different CASSIOPE passes. A2, B2, C2, and D2 are the ground-tracks referring to the measurements of A1, B1, C1, and D1 respectively. A1 was observed on 17 February, B1 was on 18 February, C1 was on 19 February, and D1 was

on 20 February 2014 during near-perigee passes. The spacecraft (**S/C) Axis** panels show the EA-t spectrograms of averaged ion count rate in the order of pixel sectors and pixel radii within the pixel sector. Anti-ram, magnetic field, and zenith directions are depicted by dashed, continuous, and dotted lines respectively. The **TOF Bin** panel shows the TOF-t spectrogram of the ion count rate. Both at bias voltage of $V_{SA} \approx -176$ V. The **Current** panel shows the measured skin current in μA and the **Counts per Second** panel shows the total ion count measured by the detector per second [Yau et al., 2015]. The ground-tracks of passes A and B are in Greenland, while C and D are also in the Arctic region at approximately the same latitudes but on the opposite side of the magnetic pole. Unfortunately other well-collocated passes were not available during this storm event. During all four passes the anti-ram pixel sector indicated the highest ion count rate, meaning ions were arriving predominantly from the ram direction. Since each of the passes occurred during early afternoon UTC the satellite was flying against the anti-sunward convection at a relatively low angle each time. The TOF Bin panels on the 19th and 20th show higher values than on the 17 and 18 which indicate the occurrence of heavier (molecular) ion species.

3. TEC Variations and Scintillation Characteristics

TEC and ROTI results derived in this work originate from using the same type of observations. GNET consists of well-distributed, high-quality geodetic GNSS receivers along the Greenland coast. The geodetic receivers readily measure the L1 and L2 phase observables at high accuracy, which allows the calculation of ROTI (see Equation (2)) without any modification to the receiver. As described in Section 2.2, S_4 values remain low under polar region conditions, but σ_φ remains unaffected. Nevertheless, we found that the internal hardware and firmware setup of the geodetic receivers make σ_φ a less than ideal choice to select as an index to characterize ionospheric activity, while our ROTI results are comparable

to the values found in the literature. The majority of the receivers operate at 1/30 Hz sampling rate, but a subset of them is capable of 1 Hz and 50 Hz modes, as well. Other researchers have shown (e.g., Jacobsen [2014]; Pi et al. [2013]) and confirmed by modern, continuous observations (e.g., SuperDARN) that the plasma convection velocity magnitude in the polar region can reach 1000 m/s or even higher speeds. This is approximately an order of magnitude larger than plasma drift speeds measured at low latitudes. Therefore, to be able to detect km-size irregularities via ROTI a minimum 1-Hz sample data rate may be needed. For the purposes of TEC mapping 1/30 Hz data appears to be sufficient, therefore the TEC we computed utilized that sampling rate. The data used in this work for ROTI calculation was sampled at 1 Hz.

Figure 4 illustrates the N_e variations over time for the entire 5-day period calculated using ground stations in Thule. Note that in Thule during this time of year the days are only approximately 4 hours long (when the sun is above the horizon) and plasma transported by convection from mid-latitudes may contribute significantly to diurnal N_e variations. The sub-regional differences in behavior of Greenlandic polar-cap TEC variations can be observed in Figures 2 and 8. The northernmost station, in Figure 2, is Thule and the southernmost is Qaqortoq. Although there are common characteristics for each station's time series (Panels 6 to 9 in Figure 2) the 19 February ionospheric storm developed somewhat differently in the different sub-regions. The largest diurnal TEC peak was shown by the Qaqortoq station (Panel 9) data on 18 February. The daily enhancement maximum is gradually decreasing as we compared even higher latitudes, with Upernavik and Thule exhibiting the lowest values deep inside the polar cap. According to the Johns Hopkins University's Auroral Particles and Imagery Display website (see unpublished data 2014, http://sd-www.jhuapl.edu/Aurora/ovation/ovation_display.html), on this day Qaqortoq was deep under the auroral oval and Sisimiut was under the pole-ward edge of it. The 18 February diurnal

cycle of ionization was interrupted at Qaqortoq and Sisimiut, when the MVTEC suddenly dropped to ~10-15 TECU from ~30 TECU. At the same time Dst and AE exhibited increased geomagnetic activities, but the PCN index remained virtually unaffected. Starting about the same time, approximately 19:00 UTC, we detected significantly increased scintillations.

The JPL GIM software was slightly modified to process GPS data. This was a consequence of a large number of cycle slips in the raw data, which resulted in too small arc sizes followed by data being discarded by the GIM algorithm. While due to certain geophysical processes the F-region was significantly depleted (discussed later in this work) after this time (see Figure 4) according to SuperDARN data the convection of plasma patches driven by the growing over-the-pole electric field remained strong. The patches propagating in the otherwise depleted ionosphere caused the significant increase in ROTI scintillations. Other researchers have proposed that TEC measurements alone are not sufficient to identify the gradients leading to scintillating conditions [e.g., Alfonsi et al., 2011], while other studies [e.g., Doherty et al., 2004] suggest that TEC gradients and scintillations often appear together. Our results demonstrate that there is no simple correlation between TEC gradients and ROTI during the storm days. Figure 10 shows typical behavior of TEC and ROTI along a single satellite IPP arc. The top panel portrays TEC gradient due to solar ionization. Superimposed on this enhancement are fluctuations of different scales and after around 14:30 UTC the TEC shows a plateau. Comparing the top panel with the middle panel it is clear that ROTI is not sensitive to regular solar ionization (in fact solar ionization tends to fill up less dense plasma regions around patches and decrease scintillations [e.g., Vickrey and Kelley, 1982; Basu et al., 1985; 1988]) but it increases significantly when the signal path intersects drifting plasma patches. The bottom panel shows the development and structure of these patches. They become significant around 13:30 UTC and clear the area with nearby IPPs by around 15:30 UTC when the IPP is near the eastern edge of the map.

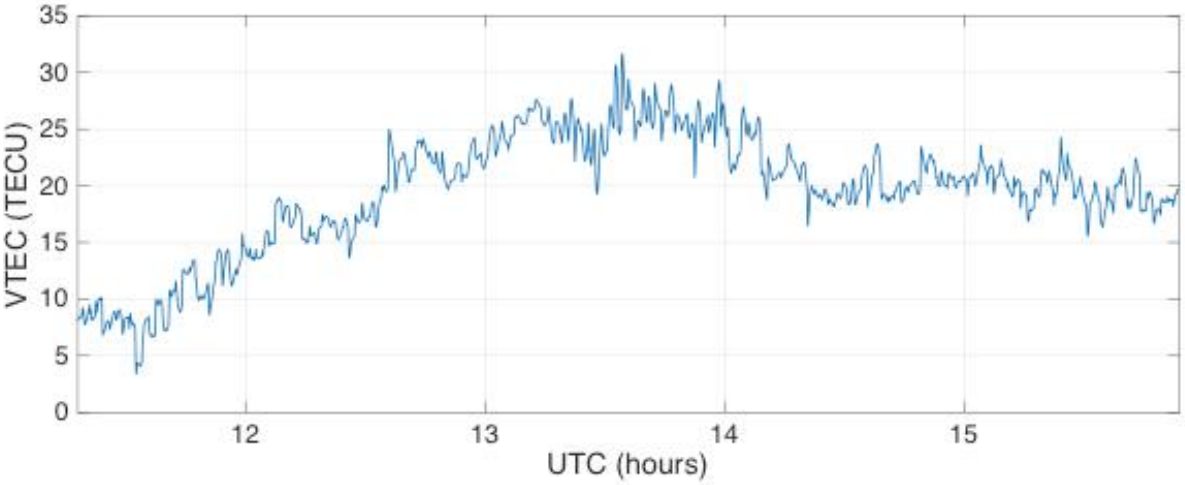

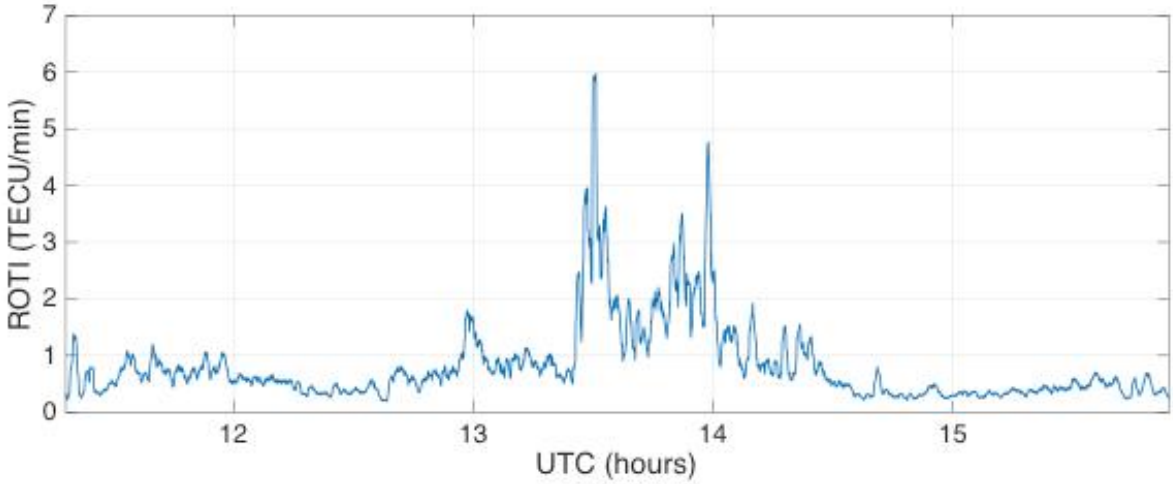

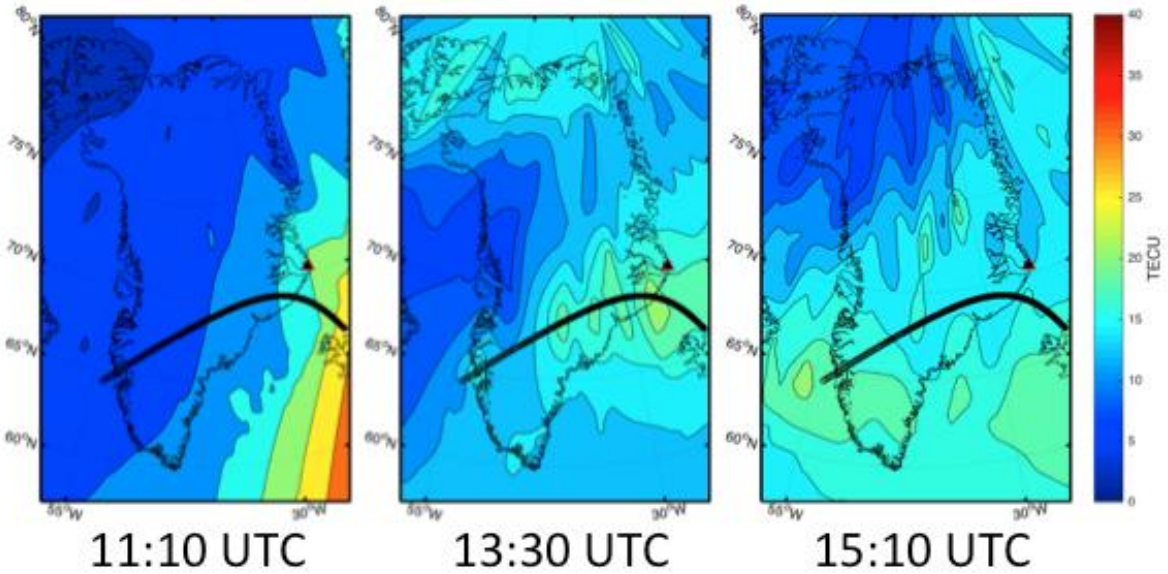

Figure 10. (top) PRN 05 (SVN 50) GPS satellite single-arc, bias-free VTEC values on 19 February 2014. Derived from Scoresbysund station data (its location is marked with black triangle on bottom panel) **(middle)** ROTI calculated for the same satelite arc. **(bottom)** Three 2D TEC maps for the same day as the top and middle panels. We used data from all 18 stations (see Figure 1) at different UTC times. The thick black line is the IPP arc for this satellite for the timespan presented in the top and middle panels.

4. Discussion

In this research we combined multi-instrument observations to investigate geophysical processes prevalent during the 19 February 2014 CME-driven geomagnetic storm in the Arctic region. We observed only one relatively small SI associated with the storm. The AE index was rising steadily starting on 18 February in association with the B_z turning southward and the Dst index decreasing until the second part of 19 February. The short recovery phase was interrupted by the arrival of a second CME, approximately 24 hours after the first one. The changes in the solar wind parameters before the first CME arrival mostly affected latitudes south of the auroral oval (Figure 2). Energy input into the polar-cap region was indicated by the sudden increase in PCN index during the early hours on 19 and 20 February. The suggested beginning of the negative storm phase occurred at the same time when the PCN index rose abruptly after 03:00 UTC on 19 February indicating that it occurred in connection with the energy input into the magnetosphere (see also Vennerstrøm et al., [1991]). The fact that this happened during local nighttime makes the pinpointing of the beginning of the negative phase more difficult; to suggest there is a negative phase the TEC decrease has to be observed during daytime hours when the ionosphere is well developed. There is a clear difference between the ionospheric behavior over polar-cap and auroral

stations. Results seen in Figure 3 further support this finding; in fact the magnetic H component has a different direction at Thule than that at the auroral stations of Kangerlussuaq and Nuuk. This implies that the Pedersen currents appear to flow in opposite directions above polar and auroral regions.

Rodger et al. [1992] summarized the most relevant geophysical processes that take part in high- and mid-latitude ionospheric structure formation. In our work, we employed a similar approach and proposed a likely geophysical explanation for the observed negative storm phase. According to Prölls et al. [1991] and Rodger et al. [1992] the formations of positive storm effects are likely caused by traveling atmospheric disturbances, change in the large-scale circulation of the thermospheric wind, penetration electric field, and equatorward shift of the auroral oval (ionization ring). Negative storm effects (e.g., depletions) are caused by agitation of the neutral gas composition and equatorward shift of the high-latitude trough region. From Figure 4 (top panel) we can conclude that the observed ionospheric storm effects take place in the F-layer. Based on Figure 4 we suggest that at least in the polar cap, the effects of precipitation on electron density are minor. According to Davies [1990] and Matuura [1972], the auroral heating during such a storm changes the atmospheric circulation that subsequently changes the composition of the neutral atmosphere, resulting in a decrease in the plasma production rate. Since this heating occurs at the bottom side of the F region (it is caused by the Pedersen current at high-latitudes; see Brekke [2013]), it will erode this region and consequently will cause depletion while increasing the hmF2 height (Figure 4). Figure 4 (top panel) also illustrates that the ionization in the polar cap during this storm occurred overwhelmingly in the F2 region. During times when the F-layer was vastly depleted (the ionization was prohibited by some process or processes) the TEC values only fluctuated around 5 to 10 TECU. Therefore, the F2-layer continuity Equation (3) can function as a starting point for the physical interpretation [Rodger et al., 1992]:

$$\frac{dN_e}{dt} = q - \beta N_e - N_e \nabla \bullet \boldsymbol{V}^{\perp} - \nabla \bullet (N_e \boldsymbol{V}^{\parallel}) \quad (3)$$

where t is time, q is the production rate, βN_e is the loss rate, $\boldsymbol{V}^{\perp}$ and $\boldsymbol{V}^{\parallel}$ are the perpendicular and parallel components of the bulk plasma velocity, respectively, with respect to the geomagnetic field. We argue that the loss-rate term on the right hand side of Equation (3) was mainly responsible for the negative storm phase, which was caused by N_2 upwelling as a result of a sudden change in the large-scale circulation of the thermospheric wind. These circulation changes cause regional or global atmospheric composition changes, and equatorward shift of the auroral oval, which are well-known occurrences during geomagnetic storms [Schunk and Nagy, 2009], as shown in Figure 9. The long term (several days long) negative effect following the negative Dst peak occurs when the local horizontal variations of velocity or ionization (this can be approximated by $N_e \nabla \bullet \boldsymbol{V}^{\perp}$ due to the high-latitude location) cause change in the plasma production processes, loss processes, or plasma transport (Equation 3). Additionally, different time histories of regions of plasmas adjacent to each other may also cause decrease in N_e [e.g., Giraud and Petit, 1978]. The present argument is supported by the apparent anomaly in the column-integrated O/N_2 ratio measurements (meaning N_2 upwelling) as seen in Figures 5 and 6. In response to large energy input at the polar-cap region dayside mid-latitude, high-density plasma convects into this region at F-region altitudes, and currents and electric field potential are increasing, which results in increased electron, ion, and neutral species temperatures due to Joule heating [Schunk and Nagy, 2009], which is demonstrated by Figure 9. The aforementioned plasma convection across the polar cap is shown in Figure 7, where SuperDARN HF radar network data is compared to high-resolution VTEC data. A continuous, but non-uniform density channel of plasma (tongue of ionization or TOI) is clearly visible, which is spatially collocated with the highest plasma velocities. The TOI eventually breaks down to polar patches as shown in

Figures 7 and 8. In the regions where the plasma is near stationary (Figure 7, left panel) N_e densities decrease as plasma decay is accelerated.

As a consequence of ionospheric heating, N_2 upwelling (also supported by the computational model of Richmond and Matsushita [1975]) is occurring, which increases the loss rate term in Equation (3). The decreased O/N_2 and heating-induced meridional neutral winds [Richmond and Matsushita, 1975] over Greenland may last for days inhibiting normal photoionization. The three most important heating mechanisms are Joule heating, ion heating, and auroral heating [Deng et al., 2008]. Heating will result in higher temperatures and thermal expansion, which will increase molecular species upwelling and plasma diffusion. The observation that the hmF2 suddenly shifted to higher altitude (by ~100-150 km), just as the CME-magnetosphere interaction started (Figures 2 and 4), supports this argument. The time-scales of Joule heating are on the order of minutes, thus they can be responsible for the sudden decrease in TEC after the initial phase. As a consequence of this, the equatorward edge of the Arctic region again becomes part of the plasmasphere, and long-term plasma densities in the plasmasphere will govern it. In order to be able to more precisely characterize and determine the atmospheric and geomagnetic processes responsible for the observed anomalies, additional observations were analyzed. IRM results from measurements during four CASSIOPE passes are shown in Figure 9. The TOF bin panels indicate that the satellite encountered more massive species after the storm (C1 and D1) than before (A1 and B1). Molecular ion species, such as NO^+, are detected at larger TOF bin values [Yau et al., 2015]. These were only negligible before the storm day. The main ion drift direction was anti-sunward during each day. Weak ion outflows were detected before the storm and virtually no ion outflow after the storm. The more massive ion presence in the topside ionosphere after the storm indicates possible upwelling.

5. Conclusions

GNSS-derived TEC and ionosonde N_e observations show negative storm effects for several days following the energy input into the polar magnetosphere by two consecutive CMEs. TEC depletion commencements seem to coincide with PCN enhancements (Figure 2).

We found that the energy input was mostly a polar-cap phenomenon (based on PCN changes in Figure 2) and it did not correlate with Dst and AE indices, which began forming disturbances several hours earlier and they would potentially indicate auroral or even lower latitude phenomena (Figures 2 and 3).

During the negative storm phase an atmospheric negative O/N_2 ratio anomaly was observed using GUVI data, which indicated N_2 upwelling and thermospheric wind changes. Ionospheric heating due to the CME's energy input during CME-driven geomagnetic activity can cause these changes in the polar atmosphere (Figures 4, 5 and 6). Polar-cap patch propagation and evolution tend to follow the expected convection patterns during negative B_z periods over the polar cap (Figures 7 and 8).

Topside sounding of ion densities and velocities using the IRM sensor showed an increase in heavier ion species during the negative storm phase following the commencement of the CME-magnetosphere interaction that seems to support the suggested heat-induced N_2 upwelling mechanism. Results from the particle detector also revealed that the topside ionosphere seems to follow the convection directions that are expected during the course of the IMF z-component turning southward (Figure 9).

Lastly, our investigations of the ROTI scintillations and comparisons with TEC maps revealed that strong scintillations mainly resulted from moving patches in the polar cap while the direct solar ionization does not appear to have had a significant influence (Figure 10). A natural way to continue this research is to explore the power-law structure of the ROTI and

TEC spectra. There are indications from previous studies, e.g., Kersley et al. [1998], that the Fresnel-frequency and the high-frequency (roll-off) slope (or sometimes slopes) of these spectra depend on the irregularity structure and drift speed. In addition to investigating the ROTI and TEC spectra, wavelet analyses could also provide a further approach to continue this research and explore the energies present in the different scale-sizes of plasma irregularities.

Acknowledgements

The authors wish to thank Lowell Digisonde International for providing access to Thule Digisonde data used in this work; the Greenland GPS Network (GNET) operated by the Technical University of Denmark, National Space Institute (DTU Space) in cooperation with the American National Science Foundation, Ohio State University, and the non-profit university governed consortium UNAVCO for GPS data; the Technical University of Denmark, National Space Institute's Geomagnetism Section for magnetometer observations; and NASA Jet Propulsion Laboratory for GIM data processing. Portions of this work were done at the Jet Propulsion Laboratory, California Institute of Technology, under a contract with NASA. NRA ROSES 2014/A.26 GNSS Remote Sensing Science Team Award is gratefully acknowledged.

The GUVI data used here were provided through support from the NASA Mission Operations and Data Analysis program. The GUVI instrument was designed and built by The Aerospace Corporation and The Johns Hopkins University. The principal investigator is Dr. Andrew B. Christensen and the chief scientist and co-PI is Dr. Larry J. Paxton.

The authors also acknowledge the use of SuperDARN convection data and CASSIOPE IRM sensor data from e-POP.

Tibor Durgonics gratefully acknowledges partial funding support for his Ph.D. program provided by activities in ESA contracts (4000105775/2012/NL/WE and 4000112279/2014/D/MRP).

Richard B. Langley acknowledges funding support from the Natural Sciences and Engineering Research Council of Canada and the Canadian Space Agency.

Data used in this paper can be obtained from the authors.

References

Alfonsi, L., L. Spogli, G. De Franceschi, V. Romano, M. Aquino, A. Dodson, and C. N. Mitchell (2011), Bipolar climatology of GPS ionospheric scintillation at solar minimum, *Radio Sci*., 46, RS0D05, doi:10.1029/2010RS004571

Anderson, B. J., S.-I. Ohtani, H. Korth, and A. Ukhorskiy (2005), Storm time dawn-dusk asymmetry of the large-scale Birkeland currents, *J. Geophys. Res*., 110, A12220, doi:10.1029/2005JA011246

Basu, S., S. Basu, E. MacKenzie, and H. E. Whitney (1985), Morphology of phase and intensity scintillations in the auroral oval and polar cap, *Radio Sci*., 20(3), 347–356, doi:10.1029/RS020i003p00347

Basu, S., E. MacKenzie, and S. Basu (1988), Ionospheric constraints on VHF/UHF communications links during solar maximum and minimum periods, *Radio Sci.*, 23, pp. 363-378, doi: 10.1029/RS023i003p00363

Bhattacharyya, A., T. L. Beach, S. Basu, and P. M. Kintner (2000), Nighttime equatorial ionosphere: GPS scintillations and differential carrier phase fluctuations, *Radio Sci*., 35(1), 209–224, doi:10.1029/1999RS002213

Blagoveshchenskii, D. V. (2013), Effect of Geomagnetic Storms (Substorms) on the Ionosphere: 1. A Review, *Geomagn. Aeron*., Vol. 53, No. 3, pp. 275-290, doi:10.1134/S0016793213030031

Brekke, A., (2013), Physics of the Upper Polar Atmosphere, 2nd ed., Springer, Heidelberg, Germany

Buonsanto, M. J. (1999), Ionospheric storms – A review, *Space Science Reviews*, 88, pp. 563-601, doi: 10.1023/A:1005107532631

Coker, C., R. Hunsucker, and G. Lott (1995), Detection of auroral activity using GPS satellites, *Geophys. Res. Lett*., 22, 23, doi:10.1029/95GL03091

Davies, K., (1990), Ionospheric Radio, Peter Peregrinus Ltd., London, UK

Deng, Y., A. J. Ridley, and W. Wang (2008), Effect of the altitudinal variation of the gravitational acceleration on the thermosphere simulation, *J. Geophys. Res*., 113, A09302, doi:10.1029/2008JA013081

Doherty, P., A. Coster, and M. Murtagh (2004), Space weather effects of October– November 2003, *GPS Solutions*, 8(4), 267, doi:10.1007/s10291-004-0109-3

Durgonics, T., G. Prates, and M. Berrocoso (2014), Detection of ionospheric signatures from GPS-derived total electron content maps, *Journal of Geodetic Science*, Vol. 4, Issue 1, doi:10.2478/jogs-2014-0011

Emmert, J. T., A. D. Richmond, and D. P. Drob (2010), A computationally compact representation of Magnetic-Apex and Quasi-Dipole coordinates with smooth base vectors, *J. Geophy. Res*., 115, A08322, doi:10.1029/2010JA015326

Feldstein, Y. I. (1986), A quarter of a century with the auroral oval, *Eos Trans*. AGU, 67(40), 761–767, doi:10.1029/EO067i040p00761-02

Ghamry, E., A. Lethy, T. Arafa-Hamed, and E. A. Elaal, A comprehensive analysis of the geomagnetic storms occurred during 18 February and 2 March 2014, NRIAG-JAG (2016) 5, 263–268, doi:10.1016/j.nrjag.2016.03.001

Giraud, A., and M. Petit (1978), Ionospheric Techniques and Phenomena, *Geophysics and Astrophysics Monographs*, 13, Springer

Gonzalez, W. D., J. A. Joselyn, Y. Kamide, H. W. Kroehl, G. Rostoker, B. T. Tsurutani, and V. M. Vasyliunas (1994), What is a geomagnetic storm?, *J. Geophys. Res*., 99(A4), 5771–5792, doi:10.1029/93JA02867

Hatch, R. R. (1982), The synergism of GPS code and carrier measurements, *J. Geod*., 57, pp. 207–208

Heelis, R. A. (1982), The polar ionosphere, *Rev. Geophys*., 20(3), 567–576, doi:10.1029/RG020i003p00567

Hernandez-Pajares, M., J. M. Juan, J. Sanz, and R. Orus (2007), Second-order ionospheric term in GPS: Implementation and impact on geodetic estimates, *J. Geophys. Res.*, 112, B08417, doi:10.1029/2006JB004707

Jacobsen, K.S. (2014), The impact of different sampling rates and calculation time intervals on ROTI values, *J. Space Weather Space Clim*., 4, A33, doi: 10.1051/swsc/2014031

Jakowski N, M. M. Hoque, and C. Mayer (2011), A new global TEC model for estimating transionospheric radio wave propagation errors, *J. Geod*, 85, 12, pp. 965-974 doi:10.1007/s00190-011-0455-1

Kersley, L., S. E. Pryse, and N. S. Wheadon (1998), Amplitude and phase scintillation at high latitudes over northern Europe, *Radio Sci*., 23, 3, doi: 10.1029/RS023i003p00320

Khazanov, G. V. (2011), Kinetic theory of the inner magnetospheric plasma, Springer-Verlag, New York, doi:10.1007/978-1-4419-6797-8

Komjathy, A. (1997). Global Ionospheric Total Electron Content Mapping Using the Global Positioning System. Ph.D. dissertation, Department of Geodesy and Geomatics Engineering Technical Report No. 188, University of New Brunswick, Fredericton, New Brunswick, Canada, 248 pp. (http://www2.unb.ca/gge/Pubs/TR188.pdf)

Komjathy, A., L. Sparks, B. D. Wilson, and A. J. Mannucci (2005a), Automated daily processing of more than 1000 ground-based GPS receivers for studying intense ionospheric storms, *Radio Sci*., 40, RS6006, doi:10.1029/2005RS003279.

Komjathy, A. A.J. Mannucci, L. Sparks, and A. Coster (2005b). ”The Ionospheric impact of the October 2003 Storm Event on WAAS.” *GPS Solutions*, (9). pp. 41-50.

Lastovicka J. (2002), Monitoring and forecasting of ionospheric space weather effects of geomagnetic storms, *J. Atmos. Sol.–Terr. Phys*., Vol. 64, pp. 697–705, doi:10.1016/S1364-6826(02)00031-7

Le, G., C. T. Russell, and K. Takahashi (2004), Morphology of the ring current derived from magnetic field observations, *Ann. Geophys.*, 22, pp. 1267-1295, doi:10.5194/angeo-22-1267-2004

Liemohn, M. W., J. U. Kozyra, M. F. Thomsen, J. L. Roeder, G. Lu, J. E. Borovsky, and T. E. Cayton (2001), Dominant role of the asymmetric ring current in producing the stormtime Dst*, *J. Geophys. Res*., 106(A6), 10883–10904, doi:10.1029/2000JA000326

Maini, A. K. and V. Agrawal (2011), Satellite Technology: Principles and Applications, John Wiley, Chichester, United Kingdom

Mannucci, A. J., B. D. Wilson, D. N. Yuan, C. H. Ho, U. J. Lindqwister, and T. F. Runge (1998), A global mapping technique for GPS-derived ionospheric total electron content measurements, *Radio Sci*., 33(3), 565–582, doi:10.1029/97RS02707

Mannucci, A.J., Iijima, B.A., Lindqwister, U.J., Pi, X.Q., Sparks, L.J., Wilson, B.D., (1999), GPS and ionosphere. In: Ross-Stone, W. (Ed.), Review of Radio Science 1996-1999, Wiley-IEEE Press, New York, ISBN: 978-0-7803-6003-7, pp. 625-665

Matuura, N. (1972), Theoretical models of ionospheric storms, *Space Sci. Rev*., 13, 1, pp. 124-189, doi:10.1007/BF00198166

Meier, R., Crowley, G., Strickland, D.J., Christensen, A.B., Paxton, L.J., Morrison, D., Hackert, C.L., (2005), First look at the 20 November 2003 superstorm with TIMED/GUVI: comparisons with a thermospheric global circulation model. *J. Geophys. Res*. 110, A09S41, http://dx.doi.org/10.1029/2004JA010990

Mendillo, M. (2006), Storms in the ionosphere: Patterns and processes for total electron content, *Rev. Geophys*., 44, RG4001, doi:10.1029/2005RG000193.

Mendillo, M., and J. A. Klobuchar (2006), Total electron content: Synthesis of past storm studies and needed future work, Radio Sci., 41, RS5S02, doi:10.1029/2005RS003394.

Mushini, S., C., E. Donovan, P. T. Jayachandran, R. B. Langley, P. Prikryl, and E. Spanswick (2014), On the relation between auroral 'scintillation' and 'phase without amplitude' scintillation: Initial investigations, IEEE Conference Publications, 2014 XXXIth URSI, DOI:10.1109/URSIGASS.2014.6929726

Paxton, L.J., A. B. Christensen, D. Morrison et al., 2004, GUVI: a hyperspectral imager for geospace. Proc. SPIE Int. Soc. Opt. Eng. 5660, 227–240, doi:10.1117/12.579171.

Pi, X., A. J. Mannucci, U. J. Lindqwister, and C. M. Ho (1997), Monitoring of global ionospheric irregularities using the Worldwide GPS Network, *Geophys. Res. Lett*, 24(18), 2283–2286, doi:10.1029/97GL02273

Pi, X., A. J. Mannucci, B. Valant-Spaight, Y. Bar-Sever, L. J. Romans, S. Skone, L. Sparks, and G. Martin Hall (2013), Observations of Global and Regional Ionospheric Irregularities and Scintillation Using GNSS Tracking Networks, Proceedings of the ION 2013 Pacific PNT Meeting, Honolulu, Hawaii, April 2013, pp. 752-761

Prikryl, P., R. Ghoddousi-Fard, L. Spogli, C. N. Mitchell, G. Li, B. Ning, P. J. Cilliers, V. Sreeja, M. Aquino, M. Terkildsen, P. T. Jayachandran, Y. Jiao, Y. T. Morton, J. M. Ruohoniemi, E. G. Thomas, Y. Zhang, A. T. Weatherwax, L. Alfonsi, G. De Franceschi, and V. Romano (2015), GPS phase scintillation at high latitudes during geomagnetic storms of 7–17 March 2012 – Part 1: The North American sector, *Ann. Geophys*., 33, 637-656, doi:10.5194/angeo-33-637-2015

Prölls, G. W. (1995), Ionospheric F-Region Storms, In Handbook of Atmospheric Electrodynamics, Vol. 2 (ed. Volland), CRC Press/Boca Raton, pp. 195-248

Prölls, G. W., L. H. Brace, H. G. Mayer, G R. Carignan, T. L. Killeen, and J. A. Klobuchar (1991), Ionospheric storm effects at subaruroral latitudes: A case study, *J. Geophys. Res*., 96, 2, pp. 1275-1288

Richmond, A. D., and S. Matsushita (1975), Thermospheric response to a magnetic substorm, *J. Geophys. Res.*, 80(19), 2839–2850, doi:10.1029/JA080i019p02839

Rodger, A. S, R. J. Moffett, and S. Quegan (1992), The role of ion drift in the formation of ionization troughs in the mid- and high-latitude ionosphere–A review, *Journal of Atmospheric and Terrestrial Physics*, Vol. 54, No. 1, pp. 1-30, doi:10.1016/0021-9169(92)90082-V

Schunk, R. and A. Nagy (2009), Ionospheres Physics, Plasma Physics, and Chemistry, 2nd ed., Cambridge University Press, Cambridge, UK

Sibson, R., 1981, A brief description of natural neighbor interpolation (Chapter 2), in V. Barnett. Interpreting Multivariate Data, pp. 21–36, John Wiley, Chichester, UK

Thomas, E. G., K. Hosokawa, J. Sakai et al. (2015), Multi-instrument, high-resolution imaging of polar cap patch trans-portation, *Radio Sci*., 50, 904–915, doi:10.1002/2015RS005672

Tsurutani, B. T. and W. D. Gonzalez, (1997), The Interplanetary Causes of Magnetic Storms: A Review, in Magnetic Storms (eds B. T. Tsurutani, W. D. Gonzalez, Y. Kamide and J. K. Arballo), American Geophysical Union, Washington, D. C.. doi: 10.1029/GM098p0077

Vennerstrøm, S., E. Friis-Christensen, O. A. Troshichev, and V. G. Andersen (1991), Comparison between the polar cap index, PC, and the auroral electrojet indices AE, AL, and AU, *J. Geophys. Res.*, 96(A1), 101–113, doi:10.1029/90JA01975

Vergados, P., A. Komjathy, T. F. Runge, M. D. Butala, and A. J. Mannucci (2016), On the characterization of the impact of GLONASS observables on the receiver bias, *Radio Sci*., doi:2015/RS005831

Verkhoglyadova, O.P., B. T. Tsurutani, A. J. Mannucci, M. G. Mlynczak, L. A. Hunt, and L. J. Paxton (2014), Ionospheric TEC, thermospheric cooling and Σ[O/N2] compositional changes during the 6–17 March 2012 magnetic storm interval (CAWSES II*), J. Atmos. Sol.-Terr. Phys*., Vol 115–116,, spp. 41–51, doi:10.1016/j.jastp.2013.11.009

Vickrey, J. F., and M. C. Kelley (1982), The effects of a conducting E layer on classical F region cross-field plasma diffusion, *J. Geophys. Res*., 87(A6), 4461–4468, doi:10.1029/JA087iA06p04461

Wei, Y., Z. Pu, M. Hong et al. (2009), Westward ionospheric electric field perturbations on the dayside associated with substorm processes, *J. Geophys. Res*., 114, A12209, doi:10.1029/2009JA014445

Yau, A.W., and H.G. James (2015), CASSIOPE Enhanced Polar Outflow Probe (e-POP) Mission Overview, *Space Sci. Rev*. doi: 10.1007/s11214-015-0135-1

Yau, A. W., A. Howarth, A. White, G. Enno, and P. Amerl (2015) Imaging and Rapid-Scanning Ion Mass Spectrometer (IRM) for the CASSIOPE e-POP Mission, *Space Sci. Rev*., 189, pp. 41-63, doi: 10.1007/s11214-015-0149-8

Zhang, Y., Paxton, L.J., Morrison, D., Wolven, B., Kil, H., Meng, C.-I., Mende, S.B., Immel, T.J., (2004), O/N2 changes during 1–4 October 2002 storms: IMAGE SI-13 and TIMED/GUVI observations. *J. Geophys. Res*. 109, A10308, http://dx.doi.org/10.1029/2004JA010441